nature

SUPPLEMENTARY INFORMATION

https://doi.org/10.1038/s41586-018-0216-x

In the format provided by the authors and unedited.

Gate-tunable frequency combs in graphene–nitride microresonators

Baicheng Yao[1,2,7,11]*, Shu-Wei Huang[1,8,11]*, Yuan Liu[3,9,11], Abhinav Kumar Vinod[1,11], Chanyeol Choi[1], Michael Hoff[1], Yongnan Li[1], Mingbin Yu[4,10], Ziying Feng[5], Dim-Lee Kwong[4,6], Yu Huang[3], Yunjiang Rao[2], Xiangfeng Duan[5]* & Chee Wei Wong[1]*

[1]Fang Lu Mesoscopic Optics and Quantum Electronics Laboratory, University of California, Los Angeles, CA, USA. [2]Key Laboratory of Optical Fiber Sensing and Communications (Education Ministry of China), University of Electronic Science and Technology of China, Chengdu, China. [3]Department of Materials Science and Engineering, University of California, Los Angeles, CA, USA. [4]Institute of Microelectronics, Singapore, Singapore. [5]Department of Chemistry and Biochemistry, University of California, Los Angeles, CA, USA. [6]Institute for Infocomm Research, Singapore, Singapore. [7]Present address: Cambridge Graphene Centre, University of Cambridge, Cambridge, UK. [8]Present address: Department of Electrical, Computer, and Energy Engineering, University of Colorado Boulder, Boulder, CO, USA. [9]Present address: School of Physics and Electronics, Hunan University, Changsha, China. [10]Present address: State Key Laboratory of Functional Materials for Informatics, Shanghai Institute of Microsystem and Information Technology, and Shanghai Industrial Technology Research Institute, Shanghai, China. [11]These authors contributed equally: Baicheng Yao, Shu-Wei Huang, Yuan Liu, Abhinav Kumar Vinod. *e-mail: yaobaicheng@uestc.edu.cn; shuwei.huang@colorado.edu; xduan@chem.ucla.edu; cheewei.wong@ucla.edu

Supplementary Information

Gate-tunable frequency combs in graphene-nitride microresonators

B. C. Yao[1,2,7*,+], S.-W. Huang[1,8*,+], Y. Liu[3,9,+], A. K. Vinod[1,+], C. Choi[1], M. Hoff[1], Y. N. Li[1], M. Yu[4,10], Z. Y. Feng[5], D.-L. Kwong[4,6], Y. Huang[3], Y. J. Rao[2], X. F. Duan[5,*] and C. W. Wong[1,*]

[1]*Fang Lu Mesoscopic Optics and Quantum Electronics Laboratory, University of California, Los Angeles, CA, USA*

[2]*Key Laboratory of Optical Fiber Sensing and Communications (Education Ministry of China), University of Electronic Science and Technology of China, Chengdu, China*

[3]*Department of Materials Science and Engineering, University of California, Los Angeles, CA, USA*

[4]*Institute of Microelectronics, Singapore 117685, Singapore*

[5]*Department of Chemistry and Biochemistry, University of California, Los Angeles, CA 90095, USA*

[6]*Institute for Infocomm Research, Singapore, Singapore*

Present Addresses:

[7]*Cambridge Graphene Centre, University of Cambridge, Cambridge, UK*

[8]*Department of Electrical, Computer, and Energy Engineering, University of Colorado Boulder, Boulder, CO, USA*

[9]*School of Physics and Electronics, Hunan University, Changsha, China*

[10]*Shanghai Institute of Microsystem and Information Technology, and Shanghai Industrial Technology Research Institute, Shanghai, China*

* yaobaicheng@uestc.edu.cn; shuwei.huang@colorado.edu; xduan@chem.ucla.edu; cheewei.wong@ucla.edu

[+] B. C. Yao, S. W. Huang, Y. Liu and A. K. Vinod contribute equally in this work.

This Supplementary Information consists of the following sections:

S1. Theoretical analysis and numerical simulations

S1.1. Principle of the dispersion modulation in graphene-silicon nitride microresonator

The carrier density of graphene is tunable via an external electrical field. Let us start with describing solely the graphene layer. During the gate tuning process, conductivity of graphene is modulated, which is written as [S1, S2]:

$$\sigma_g(f, E_F, \tau, T) = \sigma_{g,intra} + \sigma_{g,inter} = \frac{ie^2(2\pi f - i/\tau)}{\pi\hbar^2}\left\{\frac{1}{\left(2\pi f+\frac{i}{\tau}\right)^2}\int_0^\infty \varepsilon\left[\frac{\partial f_d(\epsilon)}{\partial\epsilon} - \frac{\partial f_d(-\epsilon)}{\partial\epsilon}\right]d\epsilon - \int_0^\infty\left[\frac{f_d(-\epsilon)-f_d(\epsilon)}{(2\pi f+i/\tau)^2-4(\epsilon/\hbar)^2}\right]d\epsilon\right\} \quad \text{(S1-A)}$$

Specifically,

$$\sigma_{g,intra} = \frac{ie^2E_F}{\pi\hbar(2\pi f+\frac{i}{\tau})} \quad \text{(S1-B)}$$

$$\sigma_{g,inter} = \frac{ie^2E_F}{4\pi\hbar} ln\left[\frac{2|E_F|-\hbar(2\pi f+\frac{i}{\tau})}{2|E_F|+\hbar(2\pi f+\frac{i}{\tau})}\right] \quad \text{(S1-C)}$$

Here E_F is the quasi Fermi level, directly determined by the external bias. f is the optical frequency, $\tau \approx 10^{-13}$ s is the carrier relaxation lifetime, T is the temperature, $f_d(\epsilon) = \{exp[(\epsilon-\mu)/k_BT]+1\}^{-1}$ is the Fermi-Dirac distribution, $\hbar = 1.05\times10^{-34}$ eV·s is the reduced Planck constant, $k_B = 1.3806505\times10^{-23}$J/K is the Boltzmann's constant, and $e = -1.6\times10^{-19}C$ is the unit charge.

Treating graphene as an ultrathin optical media with sheet conductivity, its effective permittivity and refractive index is determined by its complex conductivity [S3, S4, S5]:

$$\begin{cases} \epsilon_g = \frac{-\sigma_{g,i}+i\sigma_{g,r}}{2\pi f \Delta} \\ \left(n_{g,r}+in_{g,i}\right)^2 = \epsilon_{g,r}+i\epsilon_{g,i} \end{cases} \tag{S2}$$

For the media mode, $n_{g,r} > 0$ and we get the values of $n_{g,r}$ and $n_{g,i}$ as

$$\begin{cases} n_{g,r} = \frac{2\epsilon_{g,r}\left(\frac{\epsilon_{g,r}}{2}+\frac{\sqrt{{\epsilon_{g,r}}^2-{\epsilon_{g,i}}^2}}{2}\right)^{1/2} - 2\left(\frac{\epsilon_{g,r}}{2}+\frac{\sqrt{{\epsilon_{g,r}}^2-{\epsilon_{g,i}}^2}}{2}\right)^{3/2}}{\epsilon_{g,i}} \\ n_{g,i} = \left(\frac{\sqrt{{\epsilon_{g,r}}^2+{\epsilon_{g,i}}^2}}{2}-\frac{\epsilon_{g,r}}{2}\right)^{1/2} \end{cases} \tag{S3}$$

For propagating light, $n_{g,r}$ influences the phase velocity while $n_{g,i}$ refers to the propagation loss [S6]. Based on the dispersion $n_g(f, \mu)$, the gate-tunable GVD parameter of graphene D_g could be calculated:

$$\beta_m = \left(\frac{d^m\beta}{d\omega^m}\right) \tag{S4}$$

$$D_g = -\frac{2\pi c}{\lambda^2}\beta_2 = -\frac{\lambda}{c}\frac{d^2 n_{g,r}}{d\lambda^2} \tag{S5}$$

Here $\omega = 2\pi c/\lambda$, m is the order, β_2 is the GVD and β_3 is the TOD. Figure S1 plots the calculated spectra of ϵ_g, n_g and D_g, for a series of Fermi levels. With increasing Fermi level, the graphene dispersion is sizably tuned, from anomalous to normal, and then finally back to anomalous.

In this work, atomic layer graphene is deposited onto the silicon nitride waveguides. Standard optical parameters of silicon nitride waveguide are calculated in Figure S2. Figure S2a, S2b and S2c shows the group velocities, the group velocity dispersions (GVD; β_2) and the third order dispersions (TOD; β_3) of the silicon nitride waveguides. All the results are calculated based on TE polarization. Here the numbers marked in the figures are the width of the silicon nitride waveguides, with a fixed height 0.8 μm. The blue curves highlight the results of width = 1.2 μm, which is applied in our experiment.

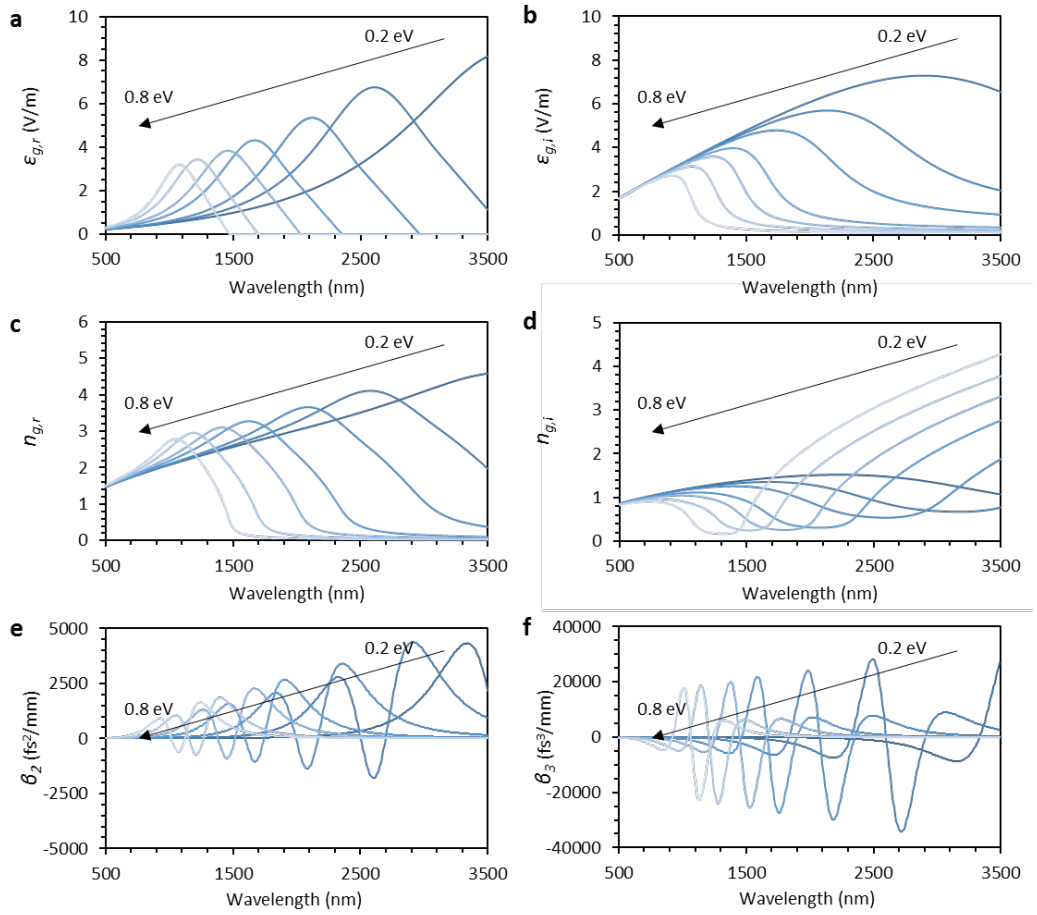

Figure S1 | Gate-tunable dispersion of graphene. a and **b,** Real part and imaginary part of the graphene permittivity, under varying from 0.2 eV to 0.8 eV (labeled from dark blue to light blue). **c** and **d,** Real part and imaginary part of the refractive index. **e,** Group velocity dispersion (GVD). **f,** Third-order dispersion (TOD).

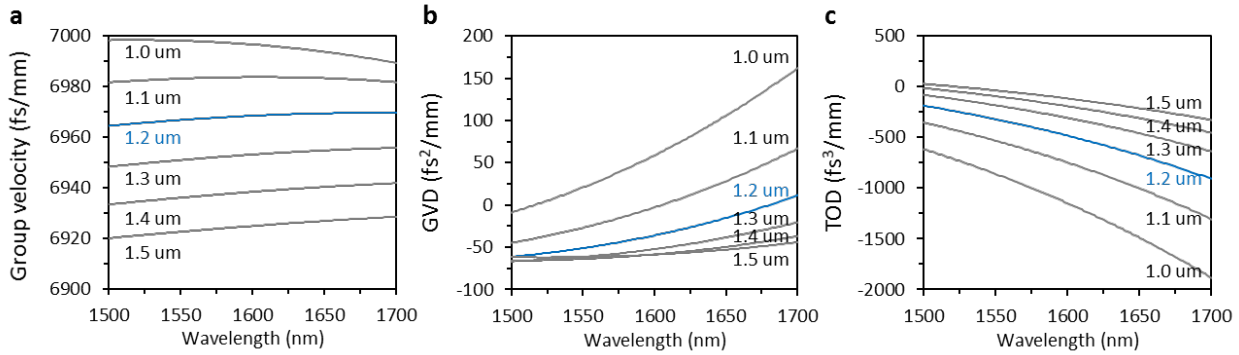

Figure S2 | Calculated optical properties of the silicon nitride waveguide, for TE polarization. **a,** group velocities. **b,** GVD. **c,** TOD. Waveguide height: 0.8 μm; waveguide width varies from 1.0 μm to 1.5 μm.

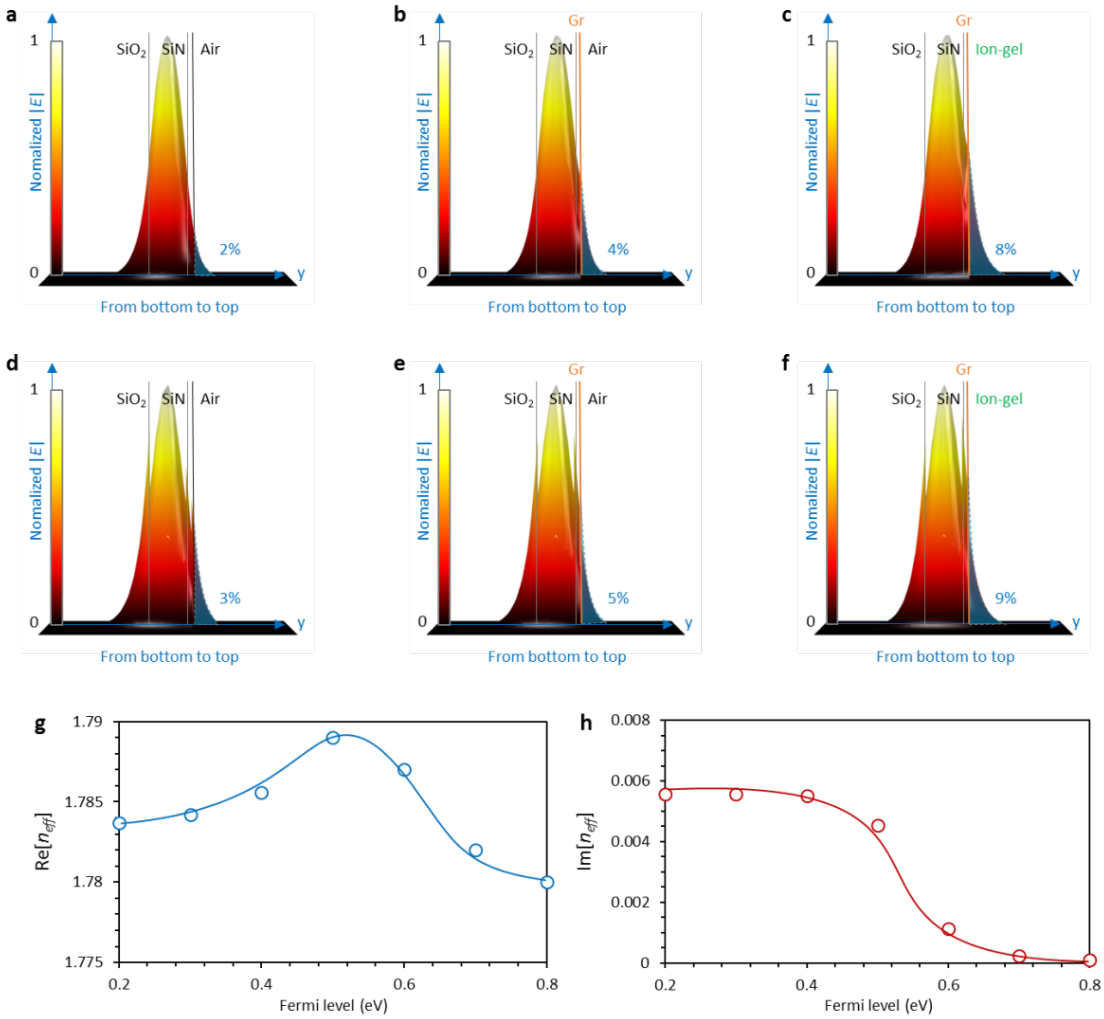

Figure S3 | Modelled |*E*|-field distributions of the heterogeneous graphene-nitride structure. **a-c,** TE_{01} mode distributions in the top etched nitride waveguide, after the graphene deposition, and after the ion-gel coverage. **d-f,** TM_{01} mode distributions in the top etched nitride waveguide, after the graphene deposition, and after the ion-gel coverage. **g-h,** During Fermi level increases from 0.2 eV to 0.8 eV, real part and imaginary part of the fundamental TE_{01} mode. In these simulations, Si_3N_4 cross-sectional size is 1200 × 800 nm^2.

By using the finite-element method, Figure S3 demonstrates the simulated |*E*|-field distributions of the silicon nitride waveguides with 1200 × 800 nm^2 core, for optical wavelength 1600 nm. Figure S3a to S3c are the simulated results of the TE_{01} mode, while Figure S3d to S3f show the TM_{01} mode. In this simulation, we fix the parameters: graphene Fermi level at 0.5 eV, graphene thickness of 0.5 nm, ion-gel thickness of 1 μm with refractive index of 1.420 [S7], silicon nitride refractive index of 1.996, silica refractive index of 1.462. Determined by the

electromagnetic boundary conditions, distributions of the TM_{01} mode are not continuous along the *y*-axis. For TE_{01} mode, before graphene deposition, ≈ 2% mode intensity distribute in the air. Afterwards, determined by the high index of graphene (3.27+i0.65 at 0.5 eV), more mode energy (≈ 4%) distributes outside, enhancing the light-graphene interaction. Finally, by covering the ion-gel on the graphene, we further increase the evanescent field distribution, up to ≈ 8% overlapping above the graphene sheet. Spatial distributions of the TM_{01} mode are similar. Enhanced by the graphene and ion-gel, mode field intensity out of the nitride/oxide waveguide increases from ≈ 3% to ≈ 9%. However, determined by the polarization dependent loss induced by scattering and absorption, Q factor of the TM_{01} mode is much lower than the TE_{01} mode. Furthermore, by modulating the n_g via gate tuning, effective index of the hybrid waveguide n_{eff} changes correspondingly [S8, S9]. Figure 3g and S3h plots the calculated effective index of the fundamental TE_{01} mode, at 1600 nm wavelength in the hybrid waveguide during the graphene Fermi level tuning from 0.2 eV to 0.8 eV.

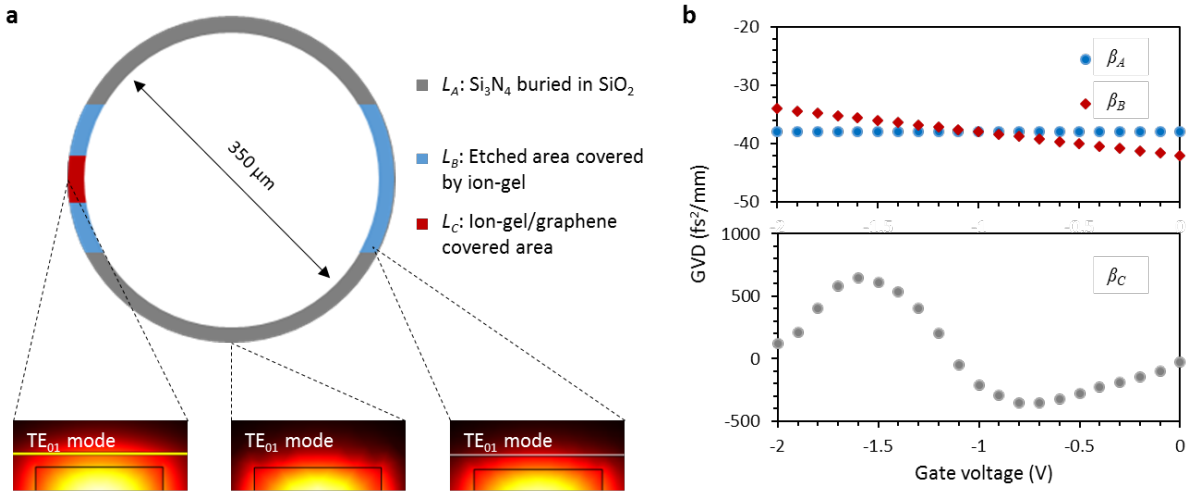

Figure S4 | Calculation of the microresonator dispersion. a, Top-view geometry of the graphene based microresonator. Three sections are marked: L_A, the nitride core buried in oxide cladding, L_B, the etched area covered by Ion-gel, L_C, the graphene heterostructured area. Inset: the TE_{01} mode in the 3 sections has different spatial patterns. **b,** Calculated GVDs of the 3 sections.

To calculate the dispersion of the whole microresonator at 1600 nm wavelength, Figure S4a shows the segmentation of the geometry. Arc lengths of L_A, L_B and L_C are ≈ 790 μm, ≈ 220 μm, and ≈ 90 μm respectively. We denote the respective GVDs as β_A, β_B, and β_C, separately

calculated with *COMSOL*. Total dispersion of the microring resonator is thus written as $\beta_2 = (\beta_A L_A + \beta_B L_B + \beta_C L_C) / (L_A + L_B + L_C)$. Figure S4b plots the calculated β_A, β_B, and β_C during the gate tuning operation, with the below three observations: **(1)** gate voltage does not affect β_A, which is kept constant around -38 fs^2/mm. **(2)** due to the ions motion and thermal heating of the ion-gel, the refractive index of the L_B section decreases slightly by ≈ 0.001 at 1600 nm [S10], with β_B increasing slightly from ≈ -42 fs^2/mm to ≈ -34 fs^2/mm in linear approximation, under gate voltage tuning from 0 V to -2 V. Compared to graphene, such a GVD modification from the ion gel and nitride temperature variation is more than two orders-of-magnitude smaller. **(3)** for the graphene/ion-gel heterostructured section, β_C oscillates dramatically compared to β_A and β_B.

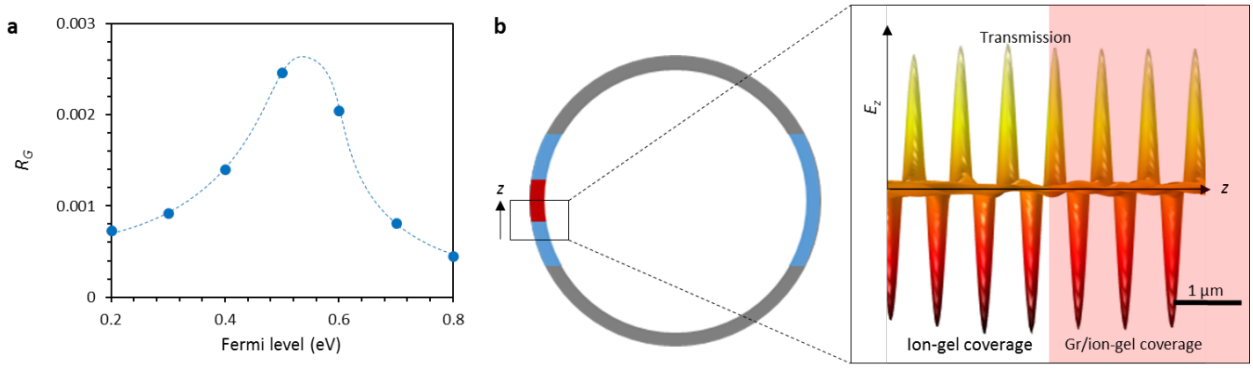

Figure S5 | Heterogeneous graphene-nitride structure induced Fresnel reflection. a, Calculated reflection ratio at the boundary of ion-gel nitride section / heterogeneous graphene-nitride, changing in range of 0.08% to 0.24% with Fermi level tuning and gate modulation. **b,** Simulated spatial waveform in the microresonator. Here *z* shows the clockwise direction.

Reflection or backward scattering in high *Q* microresonators may cause standing-wave modes [S11,S12,S13]. For frequency comb generations pumped at high power, strong standing waves which may induce hole-burning should be avoided. In our graphene heterostructured nitride microresonator, because graphene's thickness is only ≈ 5Å and the single-mode (TE_{01}) wavevector is parallel to the graphene sheet, the scattering is negligibly weak. For example, we do not observed mode-splitting in transmission and high-resolution spectral measurements on our high *Q* microresonator measurements, aided by the nitride waveguide uniformity. To further support this, Figure S5a shows our calculated reflection ratios of the TE_{01} mode, R_G, based on Fresnel equation. Determined by the Fermi level of graphene, R_G changes via gate tuning, with the highest value of R_G at 0.24% for the graphene Fermi level $|E_F|$ at ≈ 0.5 eV. Figure S5b further

simulates a waveform example (via COMSOL) along the microresonator, for $|E_F|$ = 0.5 eV, with little reflections at the graphene/ion-gel interface.

S1.2. Kerr comb generation and dispersion modulation in graphene microring resonator.

Considering that light propagates predominantly in the TE_{01} mode, Kerr comb generation in time domain is governed by the well-known nonlinear Schrodinger equation (NLSE) in graphene ring resonator [S14, S15],

$$\frac{\partial E(z,t)}{\partial z} = \frac{\alpha_L}{2}E + i\sum_{k>1}\frac{\beta_k}{k!}\left[i\frac{\partial}{\partial t}\right]^k E + i\gamma|E|^2E \qquad \text{(S6)}$$

Here α_L is the linear absorption coefficient of the resonator, $\beta_k = d^k\beta/d\omega^k \mid (\omega=\omega_0)$ are the dispersion coefficients, associated with the Taylor series expansion of the propagation constant β at center frequency ω_0. $\gamma = n_2\omega_0/cA_{eff}$ is the nonlinearity coefficient with the nonlinear refractive index n_2 and sectional-view effective modal area of the waveguide A_{eff}. Considering the comb dynamics in the cavity round trip, the NSLE is expressed in time domain [S16],

$$t_R\frac{\partial E(T,t)}{\partial T} = \left[-\alpha - i\delta_0 + iL\sum_{k>1}\frac{\beta_k}{k!}\left[i\frac{\partial}{\partial t}\right]^k E + i\gamma L|E|^2\right]E + \sqrt{\theta}E_{in} \qquad \text{(S7)}$$

Here θ is the transmission coefficient, L the is roundtrip length of the resonator, E_{in} is the input field, t_R is the roundtrip time, $\alpha = (\alpha_L+\theta)/2$ shows the total cavity loss, δ_0 is the detuning, T is the real cavity time, determined by the roundtrip as well. By using Fourier transform, Eq. (S7) could be written and solvable in frequency domain. With increasing round trips, comb lines are generated in spectrum, as shown in Figure S6 schematically. Specifically, the intensities of the comb lines are determined by the nonlinearity coefficient γ and GVD β_2, the comb line spacing is affected by the FSR, and comb bandwidth is primarily influenced by both β_2 and β_3.

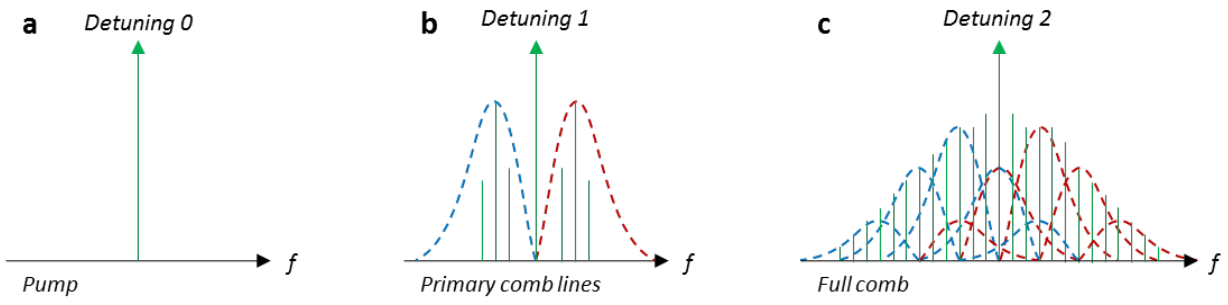

Figure S6 | Process of comb generation. a, Initially only the pump line shows in the spectrum. **b,** By changing the detuning, primary comb lines begin to appear. **c,** When the detuning meets the phase matching conditions well, the comb lines grow fully in the spectrum.

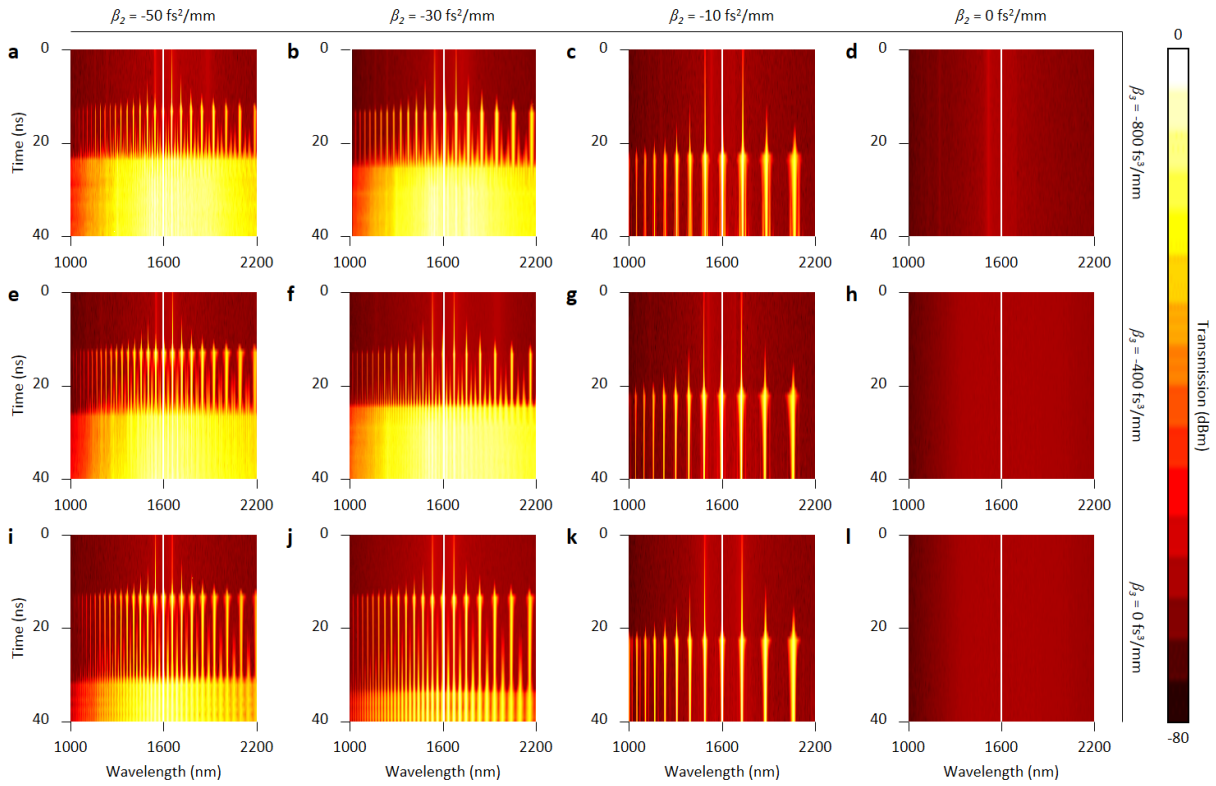

Figure S7 | Comb generation under different operating conditions. Horizon row panels: GVD increases from -50 fs^2/mm to 0 fs^2/mm. Vertical column panels: TOD increases from -800 fs^3/mm to 0 fs^3/mm.

Based on the phase matching condition, Kerr gain and energy balance, Eq. (S8) shows these relationships approximately [S17]:

$$\begin{cases} \kappa_j = \Delta k_j + 2\gamma P_j \\ P_j = \sum_{i \neq j} P_i \sqrt{4(\gamma P_i)^2 - (\kappa_i/2)^2} \\ P_0 = \sum P_j \end{cases} \tag{S8}$$

In this equation, κ_j is the phase mismatching, $\Delta k_j = \Delta k_{j,Ring} + \Delta k_{j,g}$ is the dispersion based phase mismatching, which is contributed by both the graphene and the silicon nitride ring, P_j is the power. For these parameters, j is the mode number of a comb line, and j = 0 means the input pump. This equation tells us that the dispersion modulation could be obviously measured in spectrum via checking the primary comb locations. Particularly, we can write the relative frequency difference of the generated primary lines to the pumped mode as [S18] as:

$$\Delta f = f_{FSR} \sqrt{\frac{\kappa}{\beta_2}\left(\sqrt{\frac{P_p}{P_{th}} - 1} + 1\right)} \tag{S9}$$

Here f_{FSR} is the spectral width of the FSR, β_2 is the group velocity dispersion, P_p is the pump power, and P_{th} is the threshold power. It tells that the dispersion modulation is directly captured by the movement of the primary comb lines. By scanning the detuning in a short range (5 μrad) in 0 to 40 ns, we simulate the comb generation processes of our graphene based nitride microresonator, under different β_2 and β_3, as shown in Figure S7. These simulations show the complete process how full combs are formed from the pump.

Particularly, with a fixed TOD at -800 fs^3/mm, we plot the simulated comb generation process in Figure S8. Figure S8a and S8b show the primary comb lines and the full comb at β_2 = -100 fs^2/mm. Figure S8c and S8d show the primary comb lines and the full comb at β_2 = -80 fs^2/mm. Figure S8e and S8f show the primary comb lines and the full comb at β_2 = -50 fs^2/mm. A smaller GVD results in the primary comb lines farther from the central pump, which is also observed in experiment. In above simulations, we fix the effective mode area as a 0.8 μm^2 cross-section, a pump wavelength without detuning of 1600 nm, a cavity length of the ring a 1.57 mm, a loaded quality factor of 2×10^6, and a launched power of 2 W. Referring the gate voltage based dispersion tuning, Figure S8g maps the generation of primary comb lines under V_G = -1 V, -1.2 V and -1.5 V, corresponding to Figure 3 of the main text.

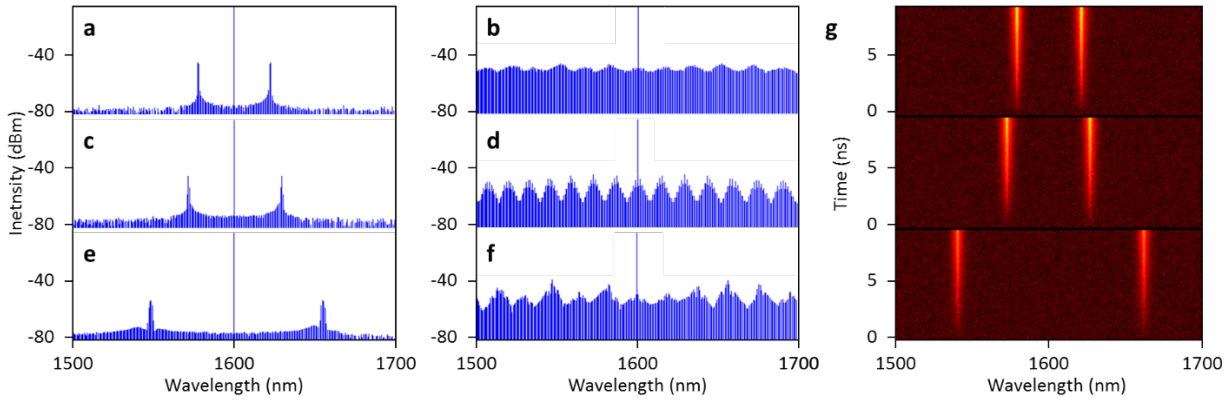

Figure S8 | Charge-tunable nonlinear microresonator comb lines. a, b, and **c,** Primary comb lines when β_2 = -100 fs^2/mm, -80 fs^2/mm, -and -50 fs^2/mm. **d**, **e,** and **f,** Full comb spectra when β_2 = -100 fs^2/mm, -80 fs^2/mm, and -50 fs^2/mm. Here the TOD is fixed at -800 fs^3/mm. **g,** gate voltage virus primary comb line location.

S1.3. Third-order nonlinearity of graphene.

It is known that graphene has a large optical nonlinearity, contributing to the four-wave mixing process [S19, S20]. The nonlinear parameter γ of the graphene ring resonator could be written as $\gamma = 3Re[2\pi f\chi^{(3)}/n_{eff}cA_{eff}]$, wherein $\chi^{(3)}$ is the third-order nonlinear susceptibility and A_{eff} is the effective mode area [S21]. Figure S9 shows the γ of graphene, the silicon nitride core, and the hybrid waveguide respectively. For $|E_F| > 0.3$ eV, a further higher Fermi level brings a lower γ [S22, S23]. Compared to silicon nitride, the third-order nonlinearity parameter of graphene is over 2 orders-of-magnitude higher. However, graphene only affects the evanescent field of the ring and hence the overall field-averaged enhancement with graphene is only slightly larger than nitride in this case: when E_F is tuned higher than 0.6 eV, γ of the hybrid waveguide is $\approx 3\times10^3$ $m^{-1}W^{-1}$.

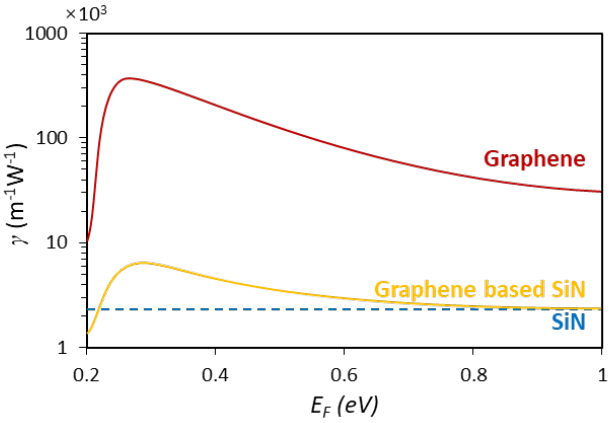

Figure S9 | Heterogeneous graphene-nitride third-order nonlinear susceptibility. Red solid line: graphene; blue dashed line: silicon nitride; gold solid line: graphene-silicon nitride hybrid.

S1.4. Cherenkov radiation and soliton generation.

Optical Cherenkov radiation, also known as dispersive wave, describes the radiation from a canonical soliton when perturbed by higher-order dispersions [S24, S25, S26]. As shown in Figure 1, not only the GVD, β_2, but also the TOD, β_3, can be tuned by changing the gate voltage to the graphene layer. Thus, the spectral peak of the Cherenkov radiation is also gate-tunable in the graphene-nitride microresonators.

For efficient energy conversion from the canonical soliton to the optical Cherenkov radiation, their propagation constants have to be matched and thus

$$\beta_s = \beta_0 + \beta_1(\omega_D - \omega_S) + \gamma P/2 = \beta_0 + \beta_1(\omega_D - \omega_S) + \sum_{N\geq 2}\frac{\beta_N(\omega_D-\omega_S)^N}{N!} = \beta_D \qquad \text{(S10)}$$

, where β_S and β_D are the propagation constants of the canonical soliton and the Cherenkov radiation respectively, γ is the nonlinear coefficient, P is the pump power, ω_S and ω_D are the center frequencies of the canonical soliton and the Cherenkov radiation respectively. Assuming the Cherenkov radiation is spectrally well separated from the canonical soliton, $\gamma P \ll \beta_2(\omega_D - \omega_S)^2$, the phase matching condition can be simplified as

$$f_D = f_S + \frac{3}{2\pi}\frac{|\beta_2|}{\beta_3} \tag{S11}$$

In the Kerr comb evolution, Turing patterns[S27, S28], chaotic states [S29] and soliton states [S30, S31] appear successively. Taking advantage of the Lugiato-Lefever mean-field model [S32], we show the difference of the Turing patterns before chaotic state and the finally formed solitons after chaotic state in Figure S10. We note that when the TOD higher than -300 fs^3/mm, it is hard to generate single soliton state by using a 600 mW on-chip pump. During the pulse evolution, multi-soliton states with versatile pulse operations are essential processes, which are also timely stable, having shown great potential in applications such as harmonic sources and ultrafast information-processes [S33, S34, S35].

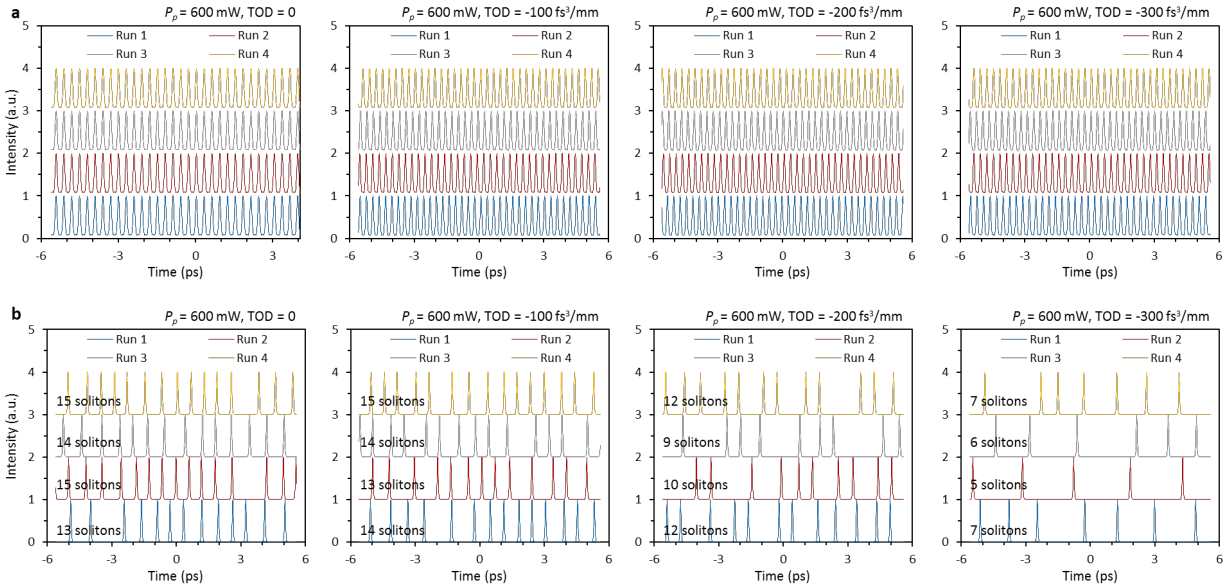

Figure S10. Simulated results of the Turing patterns and soliton generations. a, Turing patterns. **b,** Final formations of the multi-solitons. In the simulations, we use on-chip pump power 600 mW, GVD -30 fs^2/mm, intrinsic Q factor 1.061×10^6, cavity length 1.1 mm, effective mode area 1 μm^2, central wavelength 1600 nm.

Moreover, we demonstrate the simulated results of the Cherenkov soliton formations in Figure S11. Here we use TOD varying from -300 fs^3/mm to -500 fs^3/mm. Figure S10a to S10c plot the temporal profiles of the final soliton formations. Figure S10d to S10f show the statistical histograms. For TOD at -300 fs^3/mm, -400 fs^3/mm and -500 fs^3/mm, possibility of single soliton generation is estimated 0%, 44%, and 67%, respectively. The simulated results imply that for a specific GMR, single soliton tends to appear with a larger TOD and a larger pump power. For the GMR, however, a larger TOD brings higher sensitivity of GVD spectrally, which then increases the difficulty for single soliton thermal stabilization.

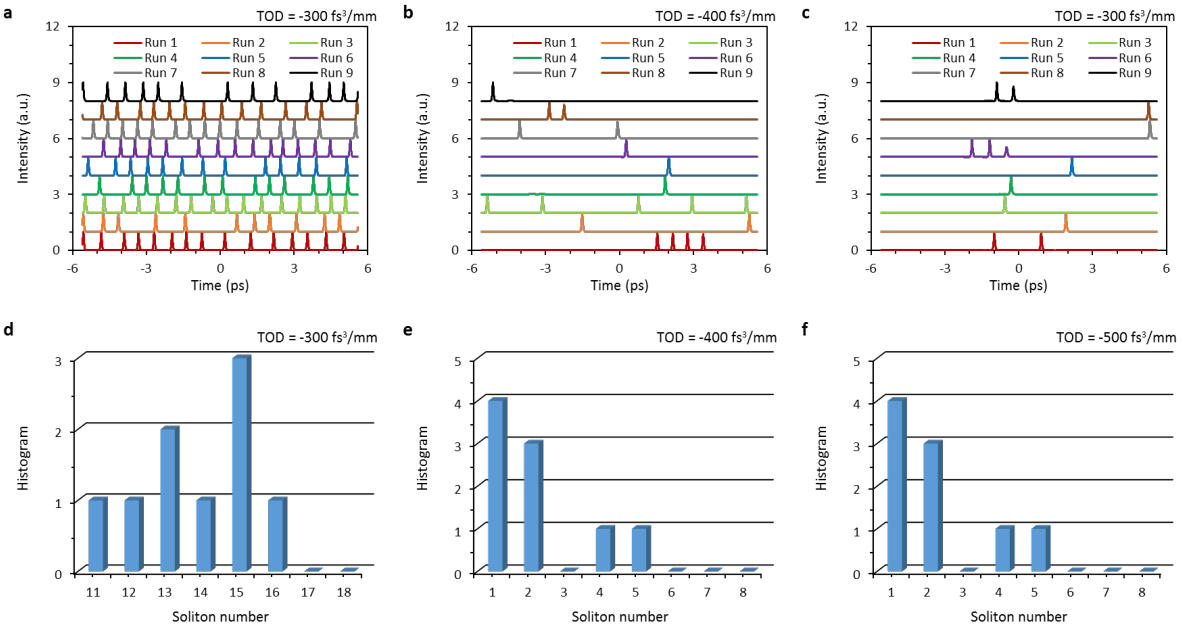

Figure S11. Numerical studies and distribution of the single-soliton states. a to **c,** Modelled soliton structures for TOD at -300 fs^3/mm, -400 fs^3/mm, and -500 fs^3/mm respectively. **d** to **f,** Occurrence distributions of the soliton numbers. In the simulations, we use a GVD of -30 fs^2/mm, an intrinsic Q factor of 1.06×10^6, a cavity length of 1.1 mm, an effective mode area of 1 μm^2, and a central pump wavelength of 1600 nm.

S2. Fabrication and baseline characterization

Figure S12 shows the fabrication process flow of the graphene-based Si_3N_4 microresonators. The microresonator has a cross-sectional 1000 × 800 nm^2 bus waveguide and a cross-sectional 1200 × 800 nm^2 core for the ring. Above the ring, there is 2500 nm thick SiO_2. First, by using standard photo-lithography followed by buffered oxide etching (7 mins), we create a photoresist

window above the ring and etched the SiO_2 to 100 nm ~ 400 nm thick for better graphene-light interaction and chromatic dispersion management.

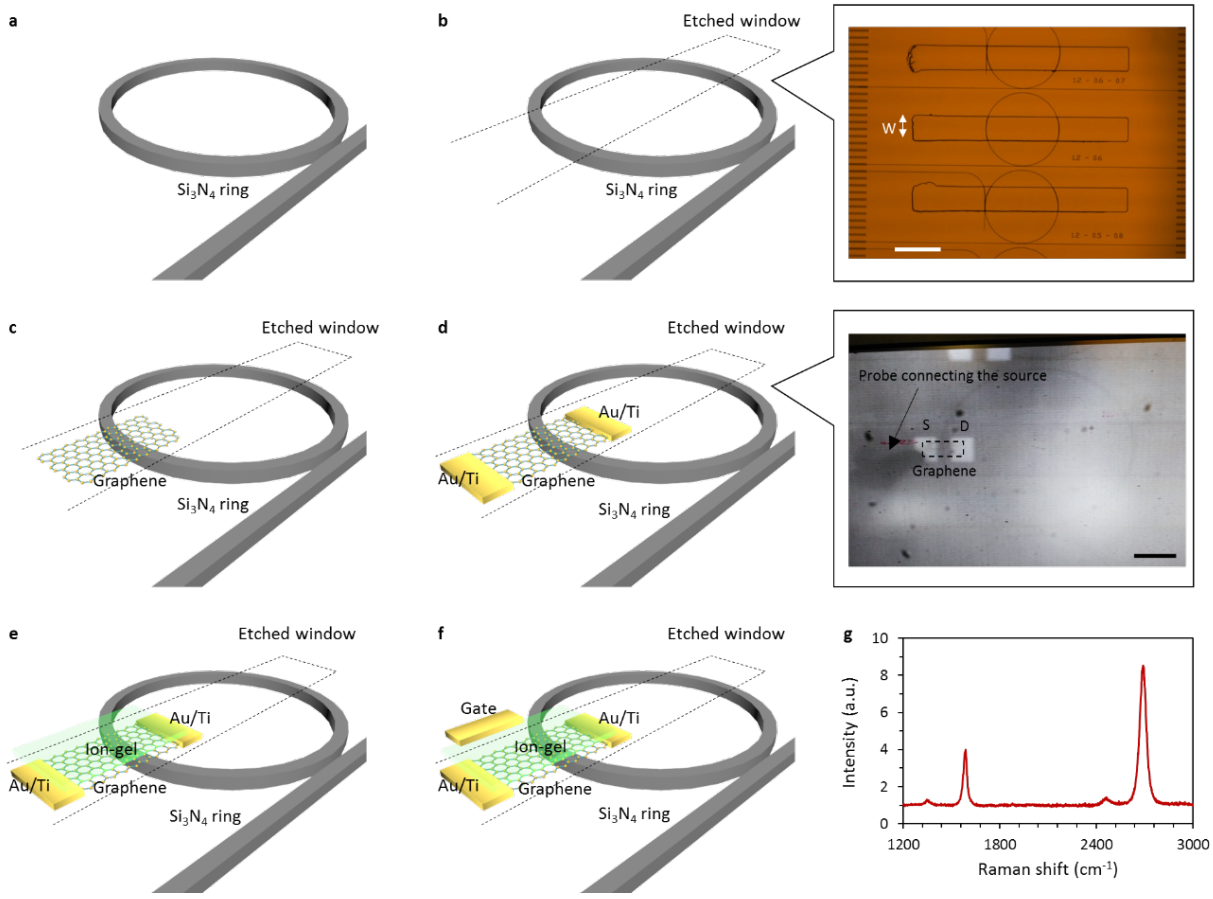

Figure S12 | Device fabrication process. a, Schematics of silicon nitride ring resonator buried in silica cladding. **b,** Schematics (left) and the top-view microscope image (right) of the chip after photolithography and oxide etching. Scale bar: 300 μm. **c,** Schematic of a monolayer graphene transferred and patterned in the etched window. **d,** Schematic (left) and top view image (right) of the device with source-drain electrodes integrated on graphene. Scale bar: 100 μm. **e,** Schematics of graphene source-drain-dielectric with a layer of ionic liquid as the gate dielectric. **f,** Schematics of device structure with gate electrode integrated. **g,** Raman spectrum of the monolayer graphene.

It is noted the edge of the ring need to be well protected by ultra-thick photoresist (~1 mm) to prevent damage from the etching process. Inset of Figure S12b shows the top-view image of the substrate with an etched oxide window. Secondly, we transfer a monolayer graphene on the etched window, followed by photolithography patterning and oxygen plasma etching, as shown

in Figure S12c. The graphene layer is grown by low pressure chemical vapor deposition (LPCVD) method on copper substrate and transferred using a modified transfer technique using PPC (polypropylene carbonate) as the protection layer. The LPCVD and PPC transfer here is essential to integrate high quality graphene on top of the ring. Next, as shown in Figure S12d, we deposit source drain electrodes (Ti/Au, 70/100 nm) using photo lithography and e-beam evaporation. Here the size of the pads is 80 μm× 60 μm. Inset of Figure S12d shows the microscope image of this step, with the chip put on the setup. Finally, we integrate ionic liquid (DEME-TFSI (N,N-diethyl-Nmethyl-N-(2-methoxyethyl) ammonium bis (trifluoromethylsulfonyl) imide, from Sigma-Aldrich) as the gate dielectric, resulting an electric double layer graphene transistor with large gate capacitance. Raman spectrum of the monolayer graphene is shown in Figure S12g, indicating the high quality of CVD grown graphene [S36].

S3. Supplementary measurements

S3.1. Experimental setup for the gate-tunable comb generation.

Figure S13a shows the experimental setup for comb generation and modulation. A tunable laser (Santec 710) with tunable range from 1480 nm to 1640 nm serves as the drive laser. It is amplified by an erbium doped fiber amplifier (EDFA, BKtel) in the L-band, working as the pump. In the experiment, the laser is tuned around 1600 nm, and the amplified power is 3.16 W (35 dBm). The pump beam is launched onto the chip via free-space. A polarization controller (PC) and a polarized beam splitter (PBS) are used to ensure the launched light is in the transverse electric (TE) mode. The graphene heterostructured microresonator (GMR) chip is fixed on a chip holder, whose temperature is controlled with a thermoelectric cooler. To tune the comb, the GMR is gated by a pair of electrical probes. For the comb spectra, the output signal is analyzed by an optical spectrum analyzer (Advantest Q8384; Yokogawa AQ6375).

Figure S13b shows the setup to gate the graphene-based resonator chip. Here two probes connect the gate and source separately. The drive laser is launched onto the chip via optimized and matched coupling lens. Figure S9c shows the image of the gated chip under an infrared camera; here the Au/Ti patterns deposited on the chip are the bright spots and the source and drain with graphene are marked by '*S*' and '*D*'. A probe inserting in the ion gel (without touching the chip) works as the top gate, marked as '*G*'. In addition, here the etched window is marked by the blue dashed box and the silicon nitride resonator is marked by the red dashed ring.

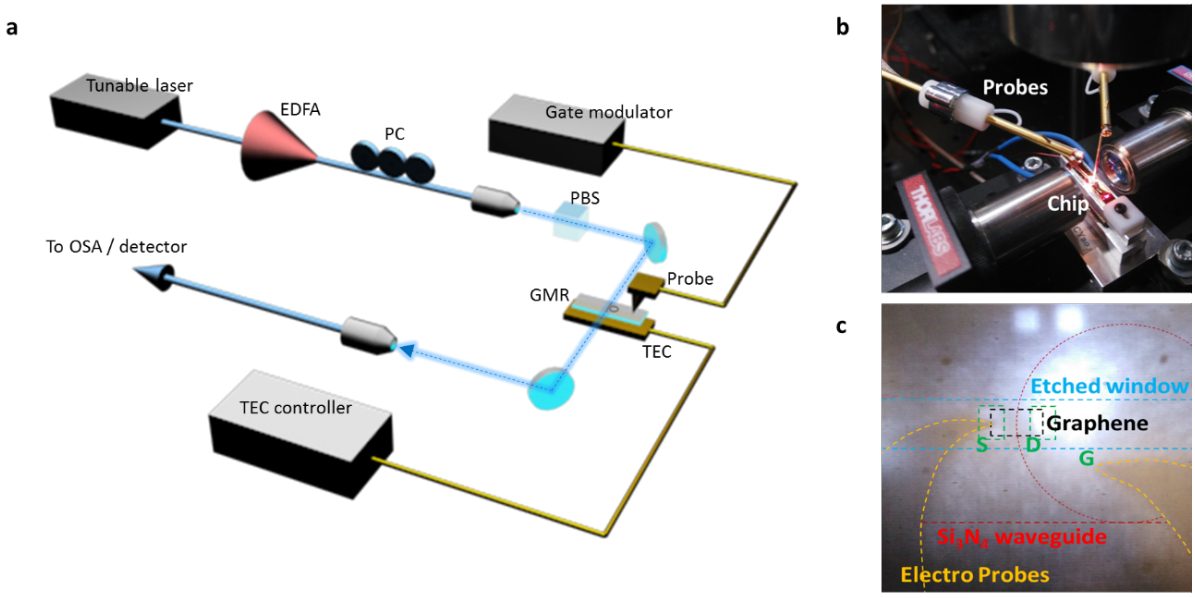

Figure S13 | Experimental arrangement. a, Schematic of the experimental setup. **b,** Probing and aligning the graphene microring resonator chip. **c,** Microscope image of the probed chip in experiment, under an infrared camera. All of the ring resonator is covered by the ion-gel. EDFA: erbium-doped fiber amplifier. PC: polarization controller. PBS: polarization beam splitter. GMR: graphene microring chip. TEC: thermoelectric cooler for chip temperature control.

S3.2. MZI-clocked dispersion measurement, with HCN optical transition referencing.

Figure S14 shows the setup for the graphene resonator transmission and dispersion measurement [S37]. The graphene microring resonator transmission is measured using a tunable laser swept through its full wavelength tuning range at 40 nm/s. Accordingly we can get its dispersion and Q factors. For accurate wavelength calibration, 1% of the laser output is directed onto a fiber-coupled hydrogen cyanide gas cell (HCN-13-100, Wavelength References) and then into a photodetector (PD 1). The graphene microring resonator and gas cell transmission are recorded during the laser sweep by a data acquisition system whose sample clock is derived from a photodetector (PD 2), monitoring the laser transmission through an unbalanced fiber Mach-Zehnder interferometer (MZI). The MZI has a determined 40 m path length difference, ensuring a measurement optical frequency sampling resolution of 5 MHz. The absolute wavelength of each sweep is determined by fitting 51 absorption features present in the gas cell transmission to determine their subsample position, assigning them to known traceable wavelengths [S38] and calculating a linear fit in order to determine the full sweep wavelength information. Each resonance is fitted with a Lorentzian lineshape unless a cluster of resonances is deemed too close

to achieve a conclusive fit with a single Lorentzian. In that case, an *N*-Lorentzian fit is utilized where *N* is the number of resonances being fitted. The dispersion of the graphene ring resonator is finally determined by analyzing the wavelength dependence of the FSR. In the setup, the graphene microring resonator chip is gated by a probe.

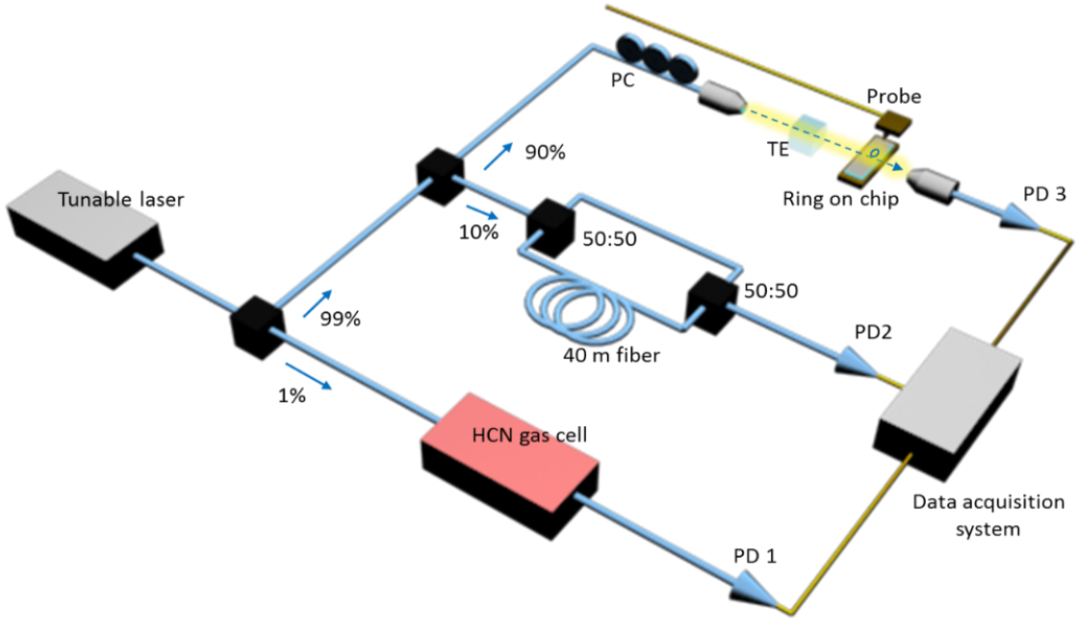

Figure S14 | Setup to quantify the dispersions and *Q* factors of the graphene microring resonators on-chip. The swept input laser is clocked with a highly-imbalanced MZI with 5 MHz optical frequency sampling resolution, and referenced against the optical transitions of a HCN reference gas cell. PC: polarization controller. TE: transverse electric mode. HCN: hydrogen cyanide. PD: photodetector.

S3.3. Heterodyne beat notes and autocorrelation measurements for soliton states.

To measure the stability and soliton states of our frequency comb, Figure S15a shows our optical heterodyne setup. We use a WDM to separate the C-band comb lines (1530 nm – 1570 nm) and the L-band comb lines (1570 nm – 1630 nm) from the pump. The 1570 nm – 1630 nm window is monitored by an OSA (Advantest AQ8384). The 1530 nm – 1570 nm spectrum beats with a stable continuous-wave (CW) laser with a narrow linewidth (300 kHz, New Focus), which serves as the heterodyne reference. A PC is used to optimize the pump polarization. The beatnotes are measured by a 3 GHz RF ESA (Agilent CXA 9000A). The comb signal is also measured in the time-domain, using a built optical intensity autocorrelator (AC). In this part, a 7 meter long dispersion-compensated fiber (DCF) along with a 15 meter long single-mode fiber is

used to compensate the GVD, avoiding the pulse broadening. Figure S15b shows the measured AC traces of our graphene based microresonator. With decreasing the pump detuning, we demonstrated the Turing patterns with dense oscillation but low extinction ratio (<3 dB), high noise state, and stable soliton states.

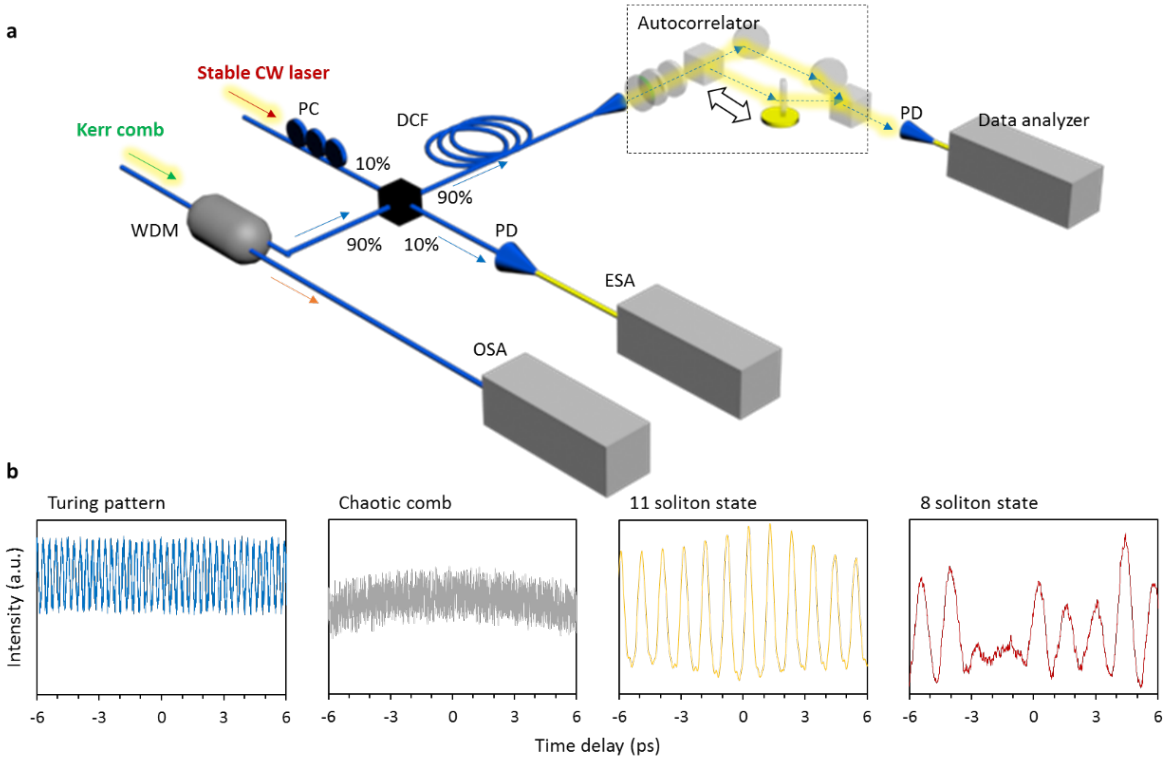

Figure S15 | Measuring the Kerr frequency comb states, with optical heterodyne and autocorrelation (AC). a, Setup: PC: polarization controller. DCF: dispersion-compensated fiber. WDM: wavelength-division multiplexer. PD: photodetector; OSA: Optical spectrum analyzer; ESA: Electric spectrum analyzer. **b,** Measured AC trace samples: from left to right, Turing, high noise, 11 soliton crystal and 8 soliton crystal.

S3.4. Measurement of the dispersion instability due to the ion dielectric.

Figure S16a shows the schematic sectional view when gating the graphene heterostructure. The gate probe is close to the graphene (height < 1 μm) while far away from the nitride core (distance > 10 μm). Mode field distribution ratio around the probes is less than 10^{-4} (Figure S4), hence the carriers in the gate probe can hardly influence the mode field. During the gate voltage tuning, the ions form an electric double layer (EDL) at the liquid/graphene interface with effective capacitance thickness ≈ 1 nm over graphene, as shown in Figure S16b schematically. The modulation speed of this graphene-EDL heterostructure is determined by both the

capacitance dynamics and ion diffusion. Stabilized by the TEC (around 323K), the capacitance response limit is under 1 MHz, which is influenced by the diffusion coefficient of the DEME-TSFI 10^{-10} m^2/s [S39, S40]. Determined by the Fick's law, diffusion time of the ions equals $x^2/2D$ approximately, here D is the diffusion coefficient, x is the average distance of the ion diffusion. In the micrometer-scale heterostructure, for graphene modulation in range of 0.59 eV to 0.62 eV, diffusion time is on hundreds ns level. Moreover, to verify the GVD modulation is induced mainly by graphene rather than ionic motion, we measured the GVD influenced by the ion-gel only. The setup is shown in Figure S16c. Here a microfiber based Mach-Zehnder interferometer (MZI) is applied to check the GVD modification. The microfiber is embedded in the ion, but far away enough from the electrodes. The diameter of the microfiber is controlled as ≈ 3 μm, ensuring ≈ 8% mode field overlapping in the ion-gel, similar to our graphene based heterostructure. GVD of the MZI is optimized at ≈ -47 fs^2/mm. By checking the FSR non-equidistance [S36], we plot correlation of the gate voltage and the GVD, in Figure S16d. GVD modification induced by the ion motion is measured to be two orders-of-magnitude smaller than in the graphene-SiN heterostructure.

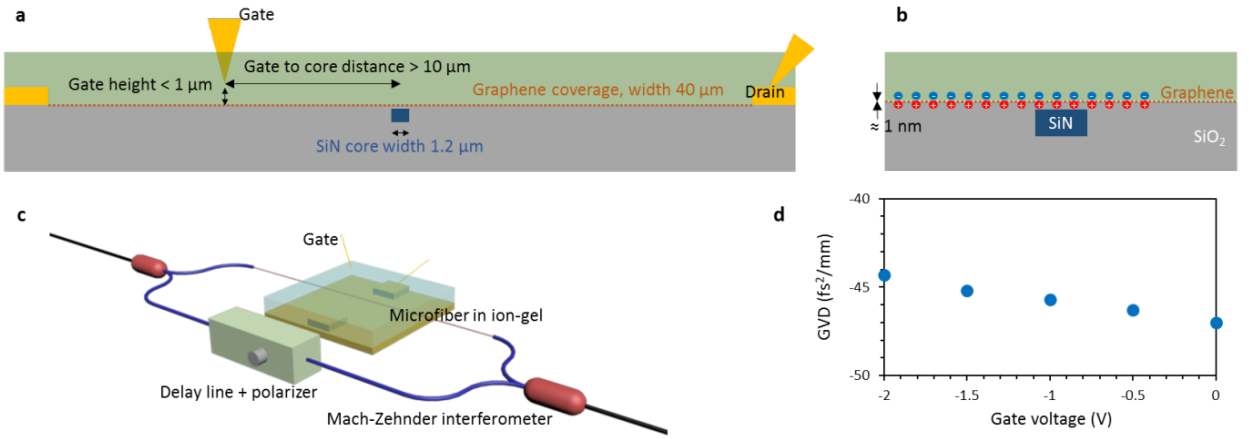

Figure S16 | Measurements of ion-gel influence on the group velocity dispersion control. a, Cross-sectional view of the heterogeneous graphene-nitride structure. **b,** Schematic diagram of the electric double layer on graphene/ion-gel interface. **c,** Mach-Zehnder setup for GVD measurement on the ion motion effects, without graphene. **d,** GVD modification induced by gating the ion-gel.

Supplementary References

S1. Mikhailov, S.& Ziegler, K. New electromagnetic mode in graphene. Phys. Rev. Lett. **99**, 016803 (2007).

S2. Hanson, G. W. Dyadic Green's functions and guided surface waves for a surface conductivity model of graphene. J. App. Phys. **103**, 064302 (2008).

S3. Vakil, A. & Engheta, N. Transformation optics using graphene, Science **332**, 1291 (2011).

S4. Lee, S. Colloidal superlattices for unnaturally high index metamaterials at broadband optical frequencies. Opt. Express **23**, 28170-28181 (2015).

S5. Yang, L. Pei, C., Shen, A., Zhao, C., Li, Y., Li, X., Yu, H., Li, Y., Jiang, X. & Yang, J. An all-optical modulation method in sub-micron scale. Sci. Rep. **5**, 9206 (2015).

S6. Yao, B, Rao, Y., Wang, Z., Wu, Y., Zhou, J., Wu, H., Fan, M., Cao, X., Zhang, W., Chen, Y., Li, Y., Churkin, D., Turitsyn, S. & Wong, C. W. Graphene based widely-tunable and singly-polarized pulse generation with random fiber lasers. Sci. Rep. **5**, 18526 (2015).

S7. Seki, S., Tsuzuki, S., Hayamizu, K., Umebayashi, Y., Serizawa, N., Takei, K. & Miyashiro, H. Comprehensive refractive index property for room-temperature ionic liquids. J. Chem. & Eng. Data **57**, 2211-2216 (2012).

S8. Sorianello, V., De Angelis, G., Cassese, T., Midrio, M., Romagnoli, M., Mohsin, M., Otto, M., Neumaier, D., Asselberghs, I., Van Campenhout, J. & Huyghebaert, C. Complex effective index in graphene-silicon waveguides. Opt. Express **24**, 29984-29993 (2016).

S9. Du, W., Li. E. & Hao, R. Tunability analysis of a graphene-embedded ring modulator. IEEE Photon. Tech. Lett. **26**, 2008 (2014).

S10. Bollinger, A., Dubuis, G., Yoon, J., Pavuna, D., Misewich, J. & Bozovic, I. Superconductor–insulator transition in $La_{2-x}Sr_xCuO_4$ at the pair quantum. Nature **472**, 458–460 (2011).

S11. Srinivasan, K. & Painter, O. Linear and nonlinear optical spectroscopy of a strongly coupled microdisk–quantum dot system. Nature **450**, 862-865 (2007).

S12. Groblacher, S. Hammerer, K., Vanner, M. R. & Aspelmeyer, M. Observation of strong coupling between a micromechanical resonator and an optical cavity field. Nature **460**, 724–727 (2009).

S13. Zhu, J., Ozdemir, S., Xiao, Y., Li, L., He, L., Chen, D. & Yang, L. On-chip single nanoparticle detection and sizing by mode splitting in an ultrahigh-*Q* microresonator. Nature Photon. **4**, 46-49 (2010).

S14. Coen, S. & Haelterman, M. Modulational instability induced by cavity boundary conditions in a normally dispersive optical fiber. Phys. Rev. Lett. **79**, 4139 (1997).

S15. Huang, S., Zhou, H., Yang, J., McMillan, J. & Matsko, A., Yu, M., Kwong, Maleki, L. & Wong, C. Mode-locked ultrashort pulse generation from on-chip normal dispersion microresonators. Phys. Rev. Lett. **114**, 053901 (2015).

S16. Coen, S., Randle, H., Sylvestre, T. & Erkintalo, M. Modeling of octave-spanning Kerr frequency combs using a generalized mean-field Lugiato–Lefever model. Opt. Lett. **38**, 37 (2013).

S17. Boyd, R. Nonlinear optics. Third Edition (Elsevier, San Diego, USA, 2003).

S18. Herr, T., Hartinger, K., Riemensberger, J., Wang, C. Y., Gavartin, E., Holzwarth, R., Gorodetsky, M. L. & Kippenberg, T. Universal formation dynamics and noise of Kerr-frequency combs in microresonators. Nature Photon. **6**, 480 (2012).

S19. Hendry, E., Hale, P., Moger, J., Savchenko, A. & Mikhailov, S. Coherent nonlinear optical response of graphene. Phy. Rev. Lett. **105**, 097401 (2010).

S20. Gu, T., Petrone, N., McMillan, J., Zande, A., Yu, M., Lo, G. Kwong, D., Hone, J. & Wong, C. Regenerative oscillation and four-wave mixing in graphene optoelectronics. Nature Photon. **6**, 554–559 (2012).

S21. Wu, Y., Yao, B., Feng, Q., Cao, X., Zhou, X., Rao, Y., Gong, Y., Zhang, W., Wang, Z., Chen, Y. & Chiang, K. Generation of cascaded four-wave-mixing with graphene-coated microfiber. Photon. Research **3**, A64 (2015).

S22. Ooi, K., Ang, L. & Tan, D. Waveguide engineering of graphene's nonlinearity. Appl. Phys. Lett. **105**, 111110 (2014).

S23. Alexander, K., Savostianova, N., Mikhailov, S., Kuyken, B. & Thourhout, D. Electrically tunable optical nonlinearities in graphene-covered SiN waveguides characterized by four-wave mixing. ACS Photonics **4**, 3039 (2017).

S24. Skryabin, D. & Gorbach, A. Colloquium: Looking at a soliton through the prism of optical supercontinuum. Rev. Mod. Phys. **82**, 1287 (2010).

S25. Erkintalo, M., Murdoch, S., Dudley, J. & Genty, G. Cascaded phase matching and nonlinear symmetry breaking in fiber frequency combs. Phys. Rev. Lett. **109**, 223904 (2012).

S26. Brasch, V., Geiselmann, M., Herr, T., Lihachev, G. Pfeiffer, M., Gorodetsky, M., & Kippenberg, T. J. Photonic chip–based optical frequency comb using soliton Cherenkov radiation. Science **351**, 357-360 (2016).

S27. Huang, S.-W., Yang, J., Yang, S.-H., Yu, M., Kwong, D.-L., Zelevinsky, T., Jarrahi, M. & Wong, C. W. Globally stable microresonator Turing pattern formation for coherent high-power THz radiation on-chip. Phys. Rev. X **7**, 041002 (2017).

S28. Coillet, A., Balakireva, I., Henriet, R., Saleh, K., Larger, L., Dudley, J. M., Menyuk, C. R. & Chembo, Y. K. Azimuthal Turing patterns, bright and dark cavity solitons in Kerr combs generated with whispering-gallery-mode resonators. IEEE Photon. **5**, 6100409 (2013).

S29. Wabnitz, S. Suppression of interactions in a phase-locked soliton optical memory. Optics Lett. **18**, 601 (1993).

S30. Herr, T., Brasch, V., Jost, J. D., Wang, C. Y., Kondratiev, N. M., Gorodetsky, M. L., & Kippenberg, T. J. Temporal solitons in optical microresonators. Nature Photonics **8**, 145 (2014).

S31. Parra-Rivas, P., Gomila, D., Matías, M. A., Coen, S. & Gelens, L. Dynamics of localized and patterned structures in the Lugiato-Lefever equation determine the stability and shape of optical frequency combs. Phys. Rev. A **89**, 043813 (2014).

S32. Huang, S., Yang, J., Yu, M., McGuyer, B. & Kwong, D. Zelevinsky, T. & Wong, C. A broadband chip-scale optical frequency synthesizer at 2.7×10^{-16} relative uncertainty. Science Adv. **2**, 1501489 (2016)..

S33. Grelu, P. & Akhmediev, N. Dissipative solitons for mode-locked lasers. Nature Photon. **6**, 84 (2012).

S34. Marin-Palomo, P., Kemal, J., Karpov, M., Kordts, A., Pfeifle, J., Pfeiffer, M., Trocha, P., Wolf, S., Brasch, V., Anderson, M., Rosenberger, R., Vijayan, K., Freude, W., Kippenberg, T. & Koos, C. Microresonator-based solitons for massively parallel coherent optical communications. Nature **546**, 274 (2017).

S35. Paccianti, M., Pasquazi, A., Park, Y., Little, B., Chu, S., Moss, D. & Morandotti, R. Demonstration of a stable ultrafast laser based on a nonlinear microcavity. Nature Comm. **3**, 765 (2012).

S36. Liu, Y., Cheng, R., Liao, L., Zhou, H., Bai, J., Liu, G., Liu, L., Huang, Y. & Duan, X. Plasmon resonance enhanced multicolour photodetection by graphene. Nature Comm. **2**, 579 (2011).

S37. Huang, S., Liu, H., Yang, J., Yu, M., Kwong, D. & Wong, C. W. Smooth and flat phase-locked Kerr frequency comb generation by higher order mode suppression. Sci. Reports **6**, 26255 (2016).

S38. Gilbert, S., Swann, W., & Wang, C. Hydrogen Cyanide H13C14N absorption reference for 1530 nm to 1565 nm wavelength calibration – SRM 2519a. Natl. Inst. Std. Technol. Spec. Publ. **260**, 137 (2005).

S39. Fujimotoa, T. & Awaga, K. Electric-double-layer field-effect transistors with ionic liquids. Phys. Chem. Chem. Phys. **15**, 8983 (2013).

S40. Sato, T., Morinaga, T., Marukane, S., Narutomi, T., Igarashi, T., Kawano, Y., Ohno, K., Fukuda, T. and Tsujii, Y. Novel solid-state polymer electrolyte of colloidal crystal decorated with ionic-liquid polymer brush. Adv. Mater. **23**, 4868 (2011).